Electrospun activated carbon nanofibers with hollow core/highly mesoporous shell structure as counter electrodes for dye-sensitized solar cells

CrossMark

Seok-Hwan Park [a,b,c], Byung-Kwan Kim [a,b,c], Wan-Jin Lee [a,b,c,*]

[a] School of Applied Chemical Engineering, Chonnam National University, Gwangju 500-757, Republic of Korea
[b] Center for Functional Nano Fine Chemicals, Chonnam National University, Gwangju 500-757, Republic of Korea
[c] Alan MacDiarmid Energy Research Institute, Chonnam National University, Gwangju 500-757, Republic of Korea

HIGHLIGHTS

- Meso-HACNF was prepared by concentric electrospinning and thermal process.
- Meso-HACNF was composed of highly mesoporous shell and hollow core.
- Highly mesoporous Meso-HACNF1 had a large surface area with mesoporous surface area.
- Meso-HACNF1 with high efficiency of 7.21% is comparable to Pt CE.

ARTICLE INFO

ABSTRACT

Activated carbon nanofibers with hollow core/highly mesoporous shell structure (Meso-HACNF) are prepared by concentric electrospinning using poly(methyl methacrylate) (PMMA) as a pyrolytic core precursor with either polyacrylonitrile (PAN) or PAN/PMMA blended polymer as a carbon shell precursor, subsequently proceeded to the process of stabilization, carbonization, and activation. Meso-HACNFs with two different PMMA concentrations, 10 wt.% and 20 wt.%, are composed of a highly mesoporous shell and hollow core while HACNF without PMMA is composed of a relatively small mesoporous shell and hollow core. Highly mesoporous Meso-HACNF1 has a large surface area of 1191 m^2 g^{-1} with a mesoporous surface area of 151 m^2 g^{-1}. Meso-HACNF1 with 10 wt.% PMMA has a high efficiency of 7.21%, and is comparable to Pt CE because of its novel characteristics, which promote the electron and ion transfer, decrease the resistance of charge transfer, and increase the contact area between liquid electrolyte and Meso-HACNF1.

© 2013 Elsevier B.V. All rights reserved.

1. Introduction

Dye-sensitized solar cells (DSSCs) have been studied widely in solving an energy problem due to their high energy conversion efficiency, simple fabrication process, and low production costs [1–3]. Generally, DSSCs consist of a TiO_2 electrode with an absorbed dye on its surface, an electrolyte with an iodine complex, and a counter electrode (CE) coated with Pt. As the most important component in DSSCs, the CE plays a crucial role in collecting electrons arriving from the external circuit and catalyzing the reduction of triiodide ion (I_3^-). Platinum, the best performing material in the CE, exhibits excellent photoelectrochemical catalytic activity for the I_3^-/I^- redox couple, but is very expensive and shows corrosive phenomena in the iodide electrolyte. To solve such a problem, various low-cost materials, such as carbonaceous materials [4–9], metal oxide [10], conductive polymers [11,12], transition metal carbides [13,14], and low cost quaternary chalcogenide materials [15] have been recommended with the object of replacing the expensive platinum. Among them, carbonaceous materials show excellent performance because of their large surface area, high electronic conductivity, corrosion resistance toward iodine, high reactivity for triiodide reduction, and low cost [16–22]. Kay and Grätzel first presented carbon CEs consisting of graphite and carbon black [23]. Specifically, considerable research concerning Pt-free carbonaceous materials counter electrode with high efficiency of more than 7% has been performed on preparing carbon nanofiber (CNF) [24], MWCNT

* Corresponding author. School of Applied Chemical Engineering, Chonnam National University, Gwangju 500-757, Republic of Korea. Tel.: +82 62 530 1895; fax: +82 62 530 1889.
E-mail addresses: wjlee@jnu.ac.kr, wjlee@chonnam.ac.kr (W.-J. Lee).

[25,26], carbon black [17], and conductive polymer/CNT composites [12]. However, the CNF has a limitation for developing highly porous structure for the effective catalytic reaction, and the MWCNT is expensive compared to other carbonaceous materials, and also the carbon black CE needs overabundant carbon black caused by large thickness in obtaining high performance [17]. Therefore, the morphology of carbonaceous materials needs to be changed to which it simultaneously possesses both excellent porous structure and 1-D conducting pathway with facile electron transfer in order to maximize the photoelectrochemical catalytic activity performance. Although the enhancement of photoelectrochemical catalytic activity using carbonaceous materials for CE of DSSCs have been studied, comparatively insignificant results about ACNF with hollow core/porous shell structure in the catalytic activity for DSSCs were reported previously.

The concentric electrospinning is a unique method that can produce carbon nanofibers with hollow core/porous shell structure [27,28]. The key factor in improving the photoelectrochemical catalytic activity of CE is to increase the specific surface area with high mesoporosity that can be developed with both concentric electrospinning and proper thermal process. In the process of concentric electrospinning, only PMMA pyrolytic polymer is added to the inner nozzle whereas both PAN carbonizing polymer and PMMA pyrolytic polymer are inserted to the outer nozzle. Upon the completion of thermal process, the decomposition of PMMA pyrolytic polymers in the inner nozzle yields to a hollow core structure while the remaining carbons from PAN polymers and pyrolyzed PMMA polymers in the outer nozzle produce a highly porous shell structure [29]. The mesopores of activated carbon nanofibers with hollow core/porous shell structure (Meso-HACNF) are shallow due to the nanosized diameter of carbon fibers and its facile catalytic activity for the I_3^-/I^- redox couple. Accordingly, Meso-HACNF possesses large surface area with high mesoporosity, 1-D electrical pathway, and facile ion transfer.

An aim in this study is to prepare activated carbon nanofibers with hollow core/highly mesoporous shell structure (Meso-HACNF) enhancing the photoelectrochemical performance by making hollow core with PMMA pyrolytic polymer and mesoporous shell with PAN/PMMA carbonizing/pyrolytic polymer through concentric electrospinning and subsequent thermal treatment. Meso-HACNF with hollow core surface and mesoporous shell surface is very suitable for reducing triiodide ions into iodide and for the facile ions transfer by increasing contact area between Meso-HACNF and liquid electrolyte.

2. Experimental

For the preparation of HACNF, 10 wt.% of poly(methyl methacrylate) (PMMA; Mw = 120,000, Aldrich Chemical Co.) as a pyrolytic core precursor and 10 wt.% of polyacrylonitrile (PAN; Mw = 150,000, Aldrich Chemical Co.) as a carbon shell precursor were separately dissolved in N,N-dimethylformamide (DMF; Aldrich Chemical Co.), respectively. Although the core sides of Meso-HACNF1 and Meso-HACNF2 are the same as that of HACNF, the compositions of shell sides are different from that of HACNF. For Meso-HACNF1 and Meso-HACNF2, 10 wt.% polymer solutions of shell sides are composed of 9 wt.% PAN/1 wt.% PMMA, and 8 wt.% PAN/2 wt.% PMMA, respectively in DMF. A concentric injection nozzle (inner nozzle: 22G, outer nozzle: 17G) shown in Fig. 1 was designed to prepare core (PMMA)/shell (PAN or PAN/PMMA) precursor nanofibers. The condition of electrospinning is the same as the previous method [30—32]. The flow rates of inner (PMMA) and outer (PAN or PAN/PMMA) spinning solutions for all samples were 1 and 1.5 ml h^{-1}, respectively. All electrospun fibers were stabilized for 1 h at 280 °C once the temperature was increased at a rate of 1 °C min^{-1} in air, carbonized for 1 h at 1000 °C in nitrogen, and subsequent activated for 30 min at 800 °C in nitrogen with the supply of 30 vol.% steam (Fig. 1). In the activating process, the distilled water for steam was supplied by 30 ml vol. syringe, and nitrogen was controlled by a mass flow controller at 200 ml min^{-1}. The morphologies of HACNF, Meso-HACNF1, and Meso-HACNF2 were observed by a field emission scanning electron microscopy (FE-SEM, S-4700, Hitachi, Japan), a Raman microscope in KBSI-Gwangju Center (inVia Reflex, Renishaw, UK) using a 633 nm excitation source, and a transmission electron microscope (TEM, JEOL, JEM-200 FX II, USA).

Before the spray, all samples including HACNF, Meso-HACNF1 and Meso-HACNF2 were grinded using a mortar for 30 min, and 0.012 g of each grinded powders were individually added into 3 g isopropanol The mixture was sonicated for 1 h to make homogeneous slurry, and was directly sprayed onto the FTO substrate with a portable spray gun connected to the air compressor for 200 s. The final thickness of HACNF CE was around 1.6 μm. For the comparison, Pt CE was prepared by the squeeze printing method with Pt paste (Platisol T/SP, Solaronix, Switzerland) on the FTO substrate, followed by annealing at 450 °C for 30 min.

The TiO$_2$ films on the FTO glass were prepared using the squeeze printing method with two kinds of TiO$_2$ pastes. A 20-nm-sized TiO2 paste (Ti-nanoxide T/SP, Solaronix, Switzerland) as a transparent
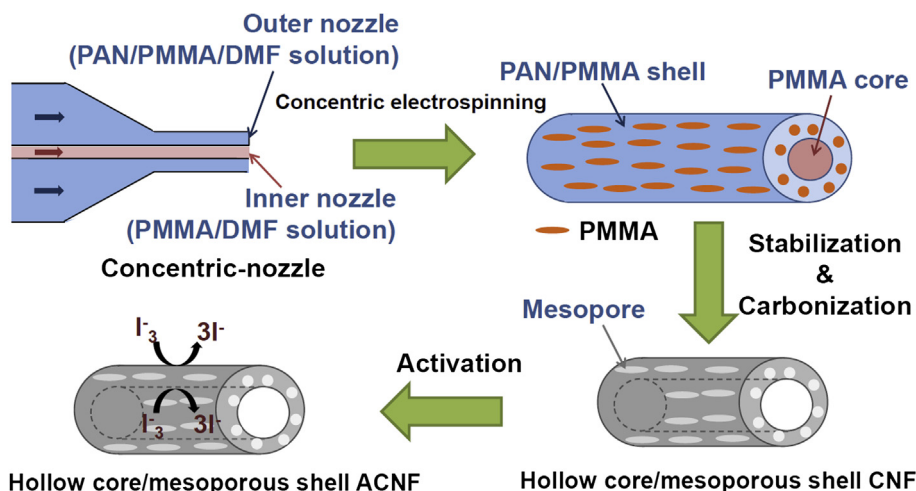

Fig. 1. The fabricating process and I_3^- reduction of activated carbon nanofiber with hollow core/mesoporous shell structure (Meso-HACNF).

layer was printed on the FTO glass, and an additional 400-nm-sized TiO_2 paste (Ti-nanoxide R/SP, Solaronix, Switzerland) was coated as the second layer of light scattering. The films were annealed at 500 °C for 30 min and then immersed into a 0.5 mM solution of N719 in ethanol for 24 h at a room temperature. The final thickness of the transparent layer is 10 μm and that of the scattering layer is 4 μm. DSSCs were assembled by employing N719-sensitized nanoporous TiO_2 electrodes and various CEs. The liquid electrolyte comprised of 0.6 M 1,2-dimethyl-3-propylimidazolium iodide, 0.1 LiI, 0.05 M I_2, 0.5 M *t*-butylpyridine and acetonitrile solvent was dropped onto the nanoporous TiO_2 film, and then the TiO_2 electrode was clipped firmly with the counter electrode. The active area of the DSSCs was 0.23 cm^2.

Cyclic voltammograms were obtained at a scan rate of 50 mV s^{-1} using a three-electrode system (counter electrode: Pt wire, reference electrode: Ag/AgCl) in an acetonitrile solution containing 0.1 M $LiClO_4$, 10 mM LiI, and 1 mM I_2. The *I–V* curves of DSSCs were measured using the electrochemistry analyzer (Compactstat.e, Ivium Technologies, Netherlands) under irradiation with a simulated solar light from a 150 W xenon arc lamp (PEC-L01, solar simulator, Peccell Technologies, Inc., Japan). The incident light

intensity was adjusted to 100 mW cm^{-2} (AM 1.5 G). The AC impedance spectra of the DSSCs were determined using the electrochemistry analyzer (Compactstat.e, Ivium Technologies, Netherlands) at the frequency range of 10 mHz–100,000 Hz with illumination. The magnitude of the alternative signal was 10 mV.

3. Results and discussion

The cross-sectional SEM and TEM images for HACNF, Meso-HACNF1, and Meso-HACNF2 are depicted in Fig. 2. In the SEM images, all of CNFs are comprised of hollow/shell structure. The core and shell diameters for all samples were approximately 200 and 360 nm, respectively. The excellent maintenance of core/shell structure over all nanofibers originates from immiscibility and thermal stability between PAN and PMMA during concentric electrospinning and thermal process [29]. For the core side, all samples produced using the method of inserting PMMA pyrolytic polymer into the inner core maintain successful hollow cores without collapsing core structures because of the immiscibility and thermal stability between PMMA of the inner core and PAN of the outer shell during concentric electrospinning and thermal process. For
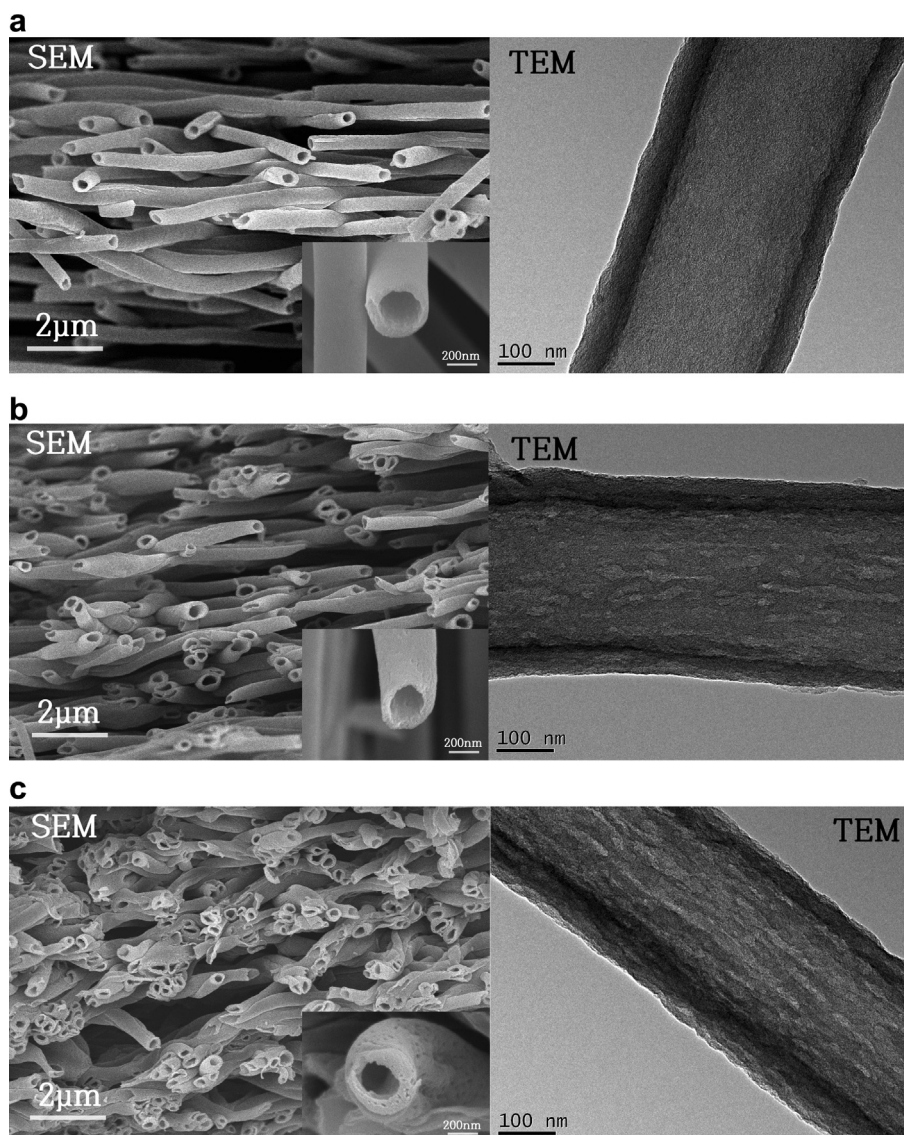

Fig. 2. The cross-sectional SEM and TEM images for (a) HACNF, (b) Meso-HACNF1, and (c) Meso-HACNF2.

the shell sides shown in TEM images of Fig. 2, HACNF forms relatively small mesoporous shell structures due to the use of only PAN carbonizing polymer while both of Meso-HACNFs reveal mesoporous shell structures due to the mixed use of PAN carbonizing polymer and PMMA pyrolytic polymer. The formation of hollow core/highly mesoporous shell structure facilitates the enhancement of photoelectrochemical performance because of its high surface area with mesoporosity.

Raman spectra for HACNF, Meso-HACNF1, and Meso-HACNF2 are illustrated in Fig. 3. The D band at 1350 cm^{-1} originates from structural disorders and defects, and the G band at 1580 cm^{-1} associates with the in-plane tangential stretch vibration mode of a perfect graphite crystal [33–35]. The D/G intensity ratio ($I_D/I_G = 0.95$) of Meso-HACNF1 is smaller than both HACNF ($I_D/I_G = 0.99$) and Meso-HACNF2 ($I_D/I_G = 1.00$). The D/G intensity ratio of carbonaceous materials commonly indicates the level of graphitization, and it is also related to the specific surface area and the average pore size of the carbon nanostructure [33,34]. As a result, the smaller D/G intensity ratio of Meso-HACNF1 demonstrates high specific surface area and mesoporous structure. The high specific surface area and mesoporous structure are beneficial to the electron transfer at the counter electrode/electrolyte interface [22]. Accordingly, the optimal combination of PAN to PMMA in the shell side can be estimated as the ratio of 9:1 rather than 8:2, which will be providing the most highly mesoporous structure.

The N$_2$ adsorption–desorption isotherms for HACNF, Meso-HACNF1, and Meso-HACNF2 is shown in Fig. 4. All samples represent a typical IV pattern confirming the evidence of mesoporous structures. The hysteresis loop by the capillary condensation of N$_2$ inside the pores is commonly caused by the existence of mesoporous structure. The hysteresis phenomena for HACNF, Meso-HACNF1, and Meso-HACNF2 represent the degree of mesoporous development, and start when the relative pressure is 0.7, 0.35, and 0.38, respectively. The inset curves of Fig. 4 indicate the BJH pore size distribution ranging from 2 to 100 nm for HACNF, Meso-HACNF1, and Meso-HACNF2. The formation of macropores at over 50 nm is ascribed to hollow core. In the mesoporous range of 2–50 nm, Meso-HACNF1 shows a tri-modal pore distribution with three distinctive peaks at around 4, 25, and 38 nm, which predicts to have a highly mesoporous structure. Also, Meso-HACNF2 with a mesoporous structure reveals a tri-modal point at around 4, 15, and 22 nm. On the other hand, HACNF has a mono-modal point at around 22 nm without a peak at the pore size of 4 nm representing relatively small mesoporous structure. The pore characteristics of HACNF, Meso-HACNF1, and Meso-HACNF2 are summarized in Table 1. Meso-HACNF1, in which the ratio of PAN to PMMA is 9:1,
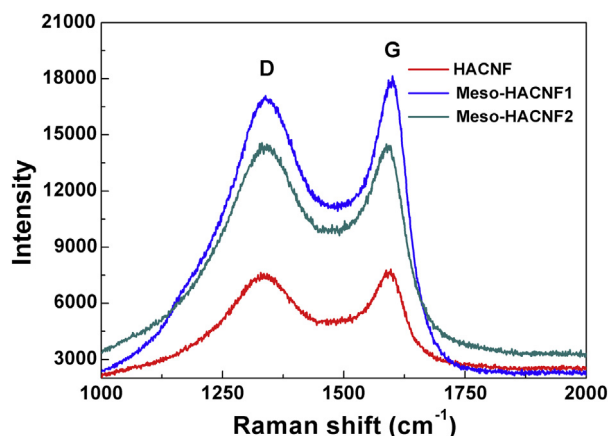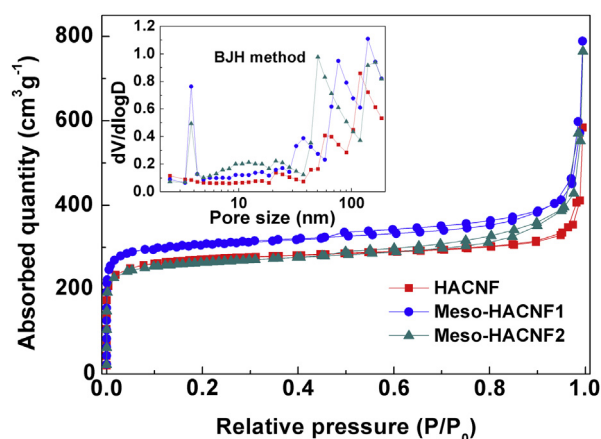

Fig. 4. N$_2$ sorption isotherms and pore size distribution of HACNF, Meso-HACNF1, and Meso-HACNF2.

shows the highest total surface area of 1191 m^2 g^{-1}, the micropore surface area of 1039 m^2 g^{-1}, and the mesopore surface area of 151 m^2 g^{-1}. Total pore volume, average pore diameter, and mesopore average diameter for Meso-HACNF1 are 0.99 cm^3 g^{-1}, 3.3 nm, and 17.9 nm, respectively. Interestingly, Meso-HACNF2, which the ratio of PAN to PMMA is 8:2, shows a decrease of total surface area to 1012 m^2 g^{-1} (micropore surface area: 867 m^2 g^{-1} and mesopore surface area: 145 m^2 g^{-1}) due to the intensive PMMA pyrolysis; however, average pore and mesopore diameters increase to 3.5 nm and 18.6 nm, respectively. On the contrary, the total surface area of HACNF is 1038 m^2 g^{-1} higher than that of Meso-HACNF2 with the micropore surface area of 940 m^2 g^{-1} and the mesopore surface area of 98 m^2 g^{-1}. The development of the optimal mesoporous structure with a large surface improves the I_3^-/I^- redox reaction rate, because mesoporous structures provide a higher possibility of liquid electrolytes to contact with carbon nanofibers.

The CVs of the I_3^-/I^- redox reaction for HACNF, Meso-HACNF1, Meso-HACNF2, and Pt CE are shown in Fig. 5. Two pairs of redox peaks are expressed in the CV curves. The pair on the left is attributed to the redox reaction (Eq. (1)), while that on the right results from the redox reaction (Eq. (2)) [36].

$$3I^- \leftrightarrow I_3^- + 2e^- \tag{1}$$

$$2I_3^- \leftrightarrow 3I_2 + 2e^- \tag{2}$$

Meso-HACNF1 represents a much larger current density of the I_3^- reduction peak than that of three other samples, due to a larger surface area with hollow core/highly mesoporous shell structure. The creation of hollow core/highly mesoporous shell structure leads to a better electrocatalytic activity with the decrease in charge transfer resistance for the I_3^-/I^- redox reaction.

The photocurrent–voltage curves of the cells with HACNF, Meso-HACNF1, Meso-HACNF2, and Pt CE is illustrated in Fig. 6. The photovoltaic parameters derived from Fig. 6 are shown in Table 2. The photovoltaic parameters of Meso-HACNF1 CE represented 7.21% energy conversion efficiency (η) with short circuit current density (J_{sc}) of 15.4 mA cm^{-2}, open circuit voltage (V_{oc}) of 0.73 V, and fill factor (FF) of 64%. The values of Meso-HACNF1 CE are comparable to that of Pt CE that showed η of 7.69, J_{sc} of 17.6, V_{oc} of 0.72, FF of 60%. The values of V_{oc} and FF for HACNF, Meso-HACNF1, and Meso-HACNF2 CE are slightly higher than those of Pt CE while the value of J_{sc} is lower. The high values of both V_{oc} and FF originate from a high surface area with mesoporous structure, and are offering the effective photocatalytic ability by the facile tri-iodide reduction [24]. On the other hand, the low value of J_{sc} attributes to higher internal

Fig. 3. Raman spectra of HACNF, Meso-HACNF1, and Meso-HACNF2.

Table 1
Pore characteristics of HACNF, Meso-HACNF1, and Meso-HACNF2.

	Micropore surface area (m^2 g^{-1})	Mesopore surface area (m^2 g^{-1})	Total surface area (m^2 g^{-1})	Total pore volume (cm^3 g^{-1})	A.P.D[a] (nm)	Mesopore avg. dia.[b] (nm)
HACNF	940	98	1038	0.70	2.7	17.4
Meso-HACNF1	1039	151	1191	0.99	3.3	17.9
Meso-HACNF2	867	145	1012	0.89	3.5	18.6

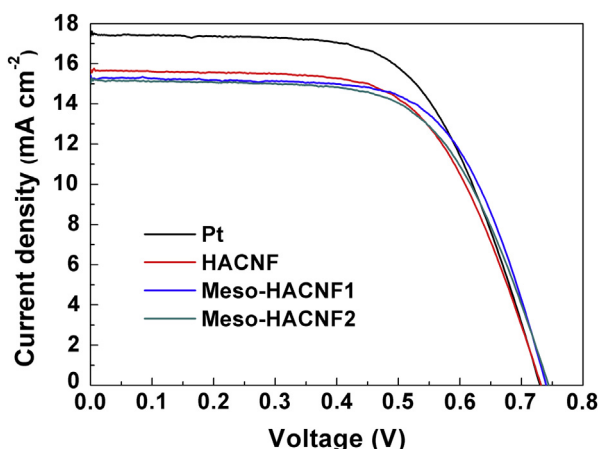[a] Average pore diameter.
[b] Calculated with 4 V A^{-1} of BJH method.
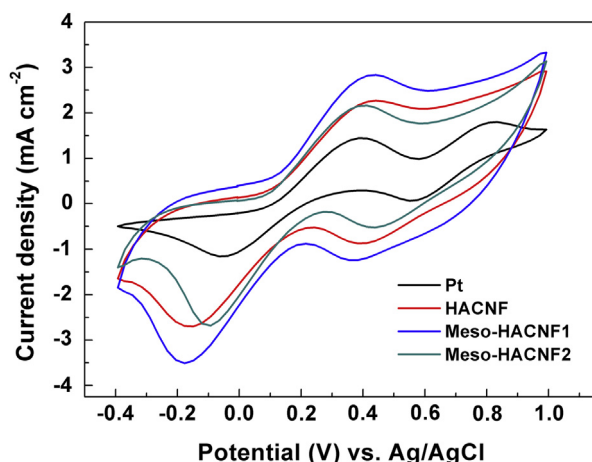
Fig. 5. Cyclic voltammograms of HACNF, Meso-HACNF1, Meso-HACNF2, and Pt counter electrode.

Table 2
Photoelectrochemical parameters of DSSCs for HACNF, Meso-HACNF1, Meso-HACNF2, and Pt counter electrode.

	J_{sc} (mA cm^{-2})	V_{oc} (V)	FF (%)	η (%)	R_s (Ω cm^2)	R_{ct} (Ω cm^2)
Pt (Reference)	17.6	0.72	60	7.69	18.0	10.9
HACNF	15.8	0.72	61	6.96	20.7	8.2
Meso-HACNF1	15.4	0.73	64	7.21	18.4	5.4
Meso-HACNF2	15.3	0.74	61	6.91	24.2	6.3

resistance due to both a large particle size and the nontransparent nature between CNF layers, which causes a light reflection to be ineffective. The improvement of photoelectrochemical performance for Meso-HACNF1 CE mainly comes from the following reasons. First, the hollow core/highly mesoporous shell structure prepared by concentric electrospinning leads to the facile charge transfer through promoting the I_3^-/I^- redox reaction rate by easily uptaking liquid electrolyte into numerous pores within the shell, hollow core, and macropores in CNF layers. Thus, the increase in contact area between Meso-HACNF1 and liquid electrolyte caused by the highly mesoporous structure promotes excellent I_3^-/I^- redox reaction [8,22]. Second, 1-D morphology of carbon nanofibers produced by concentric electrospinning facilitates charge transfer reaction with its ability to easily transfer electrons [37]. In summary, the

synergistic effect combined with excellent catalytic activity from mesoporous structure and 1-D morphology of Meso-HACNF1 facilitates higher photoelectrochemical performance by providing better internal series resistance and improving both fill factor (FF) and V_{oc} values.

Electrochemical impedance spectra (EIS) with their equivalent circuit for HACNF, Meso-HACNF1, Meso-HACNF2, and Pt CE are analyzed in Fig. 7. The charge transfer resistance (R_{ct}) of the semicircle on the high frequency region represents catalytic activity for reducing triiodide ions. The R_{ct} for all samples are ranked as follows: Meso-HACNF1 (5.4 Ω cm^2) > Meso-HACNF2 (6.3 Ω cm^2) > HACNF (8.2 Ω cm^2) > Pt (10.9 Ω cm^2). The value of R_{ct} for Meso-HACNF1 is two times lower than that of Pt. This is why Meso-HACNF1 offers a higher catalytic performance initiated from higher surface area with hollow core/highly mesoporous shell structure, and 1-D morphology of carbon nanofibers. In the equivalent circuit, Nernst diffusion impedance (Z_w) in the low frequency region for I_3^-/I^- redox species of the electrolyte is closely related to the contact between the liquid electrolyte and the surface of carbon. Compared to Meso-HACNF2 and HACNF, Meso-HACNF1 with hollow core/highly mesoporous shell structure contacts with the liquid electrolyte much easier facilitating the I_3^-/I^- redox reaction rate [8]. Such an intimate contact leads to the improvement of fill factor (FF). In other words, the FF is not only related to both charge transfers resistance

Fig. 6. I–V curves of HACNF, Meso-HACNF1, Meso-HACNF2, and Pt counter electrode.
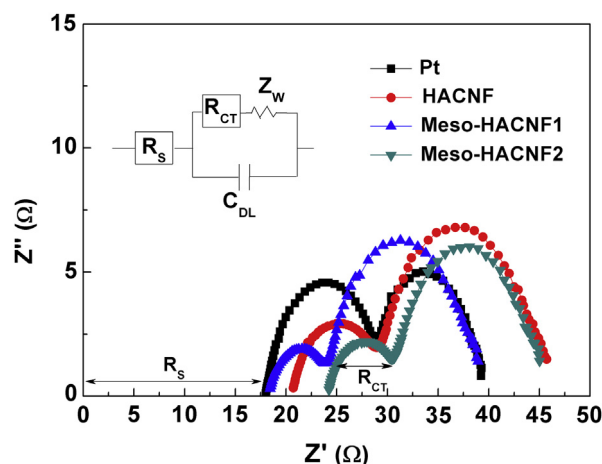
Fig. 7. EIS spectra of HACNF, Meso-HACNF1, Meso-HACNF2, and Pt counter electrode.

(R_{ct}) and diffusion resistance (Z_w), but also both sheet resistance and internal serial resistance [12,38]. On the contrary, Z_w of thick CNF electrodes prepared through spraying is higher than that of Pt CE, because Z_w increases proportionally with the thickness of CE. The internal serial resistance (R_s) is the onset point of the first semicircle for the high frequency region. The R_s represents mainly the sum of the sheet resistance of the FTO glass substrate and the contact resistance of the counter electrode. Thus, R_s of all HACNFs are higher than that of Pt CE, due to the high electrical conductivity of Pt.

4. Conclusion

Meso-HACNF1 with hollow core/highly mesoporous shell structure were successfully prepared through concentric electrospinning and subsequent thermal process. The excellent maintenance of core/shell structure over all nanofibers results from the immiscibility and thermal stability between PAN and PMMA. Meso-HACNFs possess mesoporous shell structure due to the mixed use of PAN carbonizing polymer and PMMA pyrolytic polymer. The core and shell diameters for all samples were approximately 200 and 360 nm, respectively. Meso-HACNF1 with highly mesoporous structure had the total surface area of 1191 m^2 g^{-1} with the mesoporous surface area of 151 m^2 g^{-1}, and the total pore volume of 0.99 m^2 g^{-1}. The shallowness of Meso-HACNF caused by nanosized diameters makes the catalytic activity facile. The energy conversion efficiency (7.21%) for Meso-HACNF1 CE is comparable to that of Pt CE (7.69%). The R_{ct} of Meso-HACNF1 was the smallest with the value of 5.4 Ω cm^2 due to its higher catalytic performance, which originated from high surface area and 1-D conducting pathway.

References

[1] B. O'Regan, M. Grätzel, Nature 353 (1991) 737—740.
[2] M.K. Nazeeruddin, A. Kay, I. Rodicio, R. Humphry-Baker, E. Mueller, P. Liska, N. Vlachopoulos, M. Grätzel, J. Am. Chem. Soc. 115 (1993) 6382—6390.
[3] M. Grätzel, J. Photochem. Photobiol. A 164 (2004) 3—14.
[4] E. Ramasamy, W.J. Lee, D.Y. Lee, J.S. Song, Appl. Phys. Lett. 90 (2007) 173103.
[5] W.J. Lee, E. Ramasamya, D.Y. Lee, J.S. Song, Sol. Energy Mater. Sol. Cells 92 (2008) 814—818.
[6] C.T. Hsieh, B.H. Yang, J.Y. Lin, Carbon 49 (2011) 3092—3097.
[7] K.X. Li, Y.H. Luo, Z.X. Yu, M.H. Deng, D.M. Li, Q.B. Meng, Electrochem. Commun. 11 (2009) 1346—1349.
[8] G. Wang, W. Xing, S. Zhuo, J. Power Sources 194 (2009) 568—573.
[9] D.W. Zhang, X.D. Li, H.B. Li, S. Chen, Z. Sun, X.J. Yin, S.M. Huanga, Carbon 49 (2011) 5382—5388.
[10] M. Wu, X. Lin, A. Hagfeldt, T. Ma, Chem. Commun. 47 (2011) 4535—4537.
[11] J. Chen, B. Li, J. Zheng, J. Zhao, H. Jing, Z. Zhu, Electrochim. Acta 56 (2011) 4624—4630.
[12] S. Peng, Y. Wu, P. Zhu, V. Thavasi, S.G. Mhaisalkar, S. Ramakrishna, J. Photochem. Photobiol. A 223 (2011) 97—102.
[13] M. Wu, X. Lin, A. Hagfldt, T. Ma, Angew. Chem. Int. Ed. 50 (2011) 3520—3524.
[14] J.S. Jang, D.J. Ham, E. Ramasamy, J.W. Lee, J.S. Lee, Chem. Commun. 46 (2010) 8600—8602.
[15] X. Xin, M. He, W. Han, J. Jung, Z. Lin, Angew. Chem. Int. Ed. 50 (2011) 11739—11742.
[16] Z. Huang, X. Liu, K. Li, Y. Luo, H. Li, W. Song, L. Chen, Q. Meng, Electrochem. Commun. 9 (2007) 596—598.
[17] T.N. Murakami, S. Ito, Q. Wang, M.K. Nazeeruddin, T. Bessho, I. Cesar, P. Liska, R. Humphry-Baker, P. Comte, M. Grätzel, J. Electrochem. Soc. 153 (2006) A2255—A2261.
[18] W.I. Lee, E. Ramasamy, D.Y. Lee, J.S. Song, J. Photochem. Photobiol. A 194 (2008) 27—30.
[19] K. Suzuki, M. Yamamoto, M. Kumagai, S. Yanagida, Chem. Lett. 32 (2003) 28—29.
[20] S.U. Lee, W.S. Choi, B.Y. Hong, Sol. Energy Mater. Sol. Cells 94 (2010) 680—685.
[21] K. Imoto, K. Takatashi, T. Yamaguchi, T. Komura, J. Nakamura, K. Murata, Sol. Energy Mater. Sol. Cells 79 (2003) 459—469.
[22] G. Wang, C. Huang, W. Xing, S. Zhuo, Electrochim. Acta 56 (2011) 5459—5463.
[23] A. Kay, M. Grätzel, Sol. Energy Mater. Sol. Cells 44 (1996) 99—117.
[24] G. Veerappan, W. Kwon, S.W. Rhee, J. Power Sources 196 (2011) 10798—10805.
[25] W.J. Lee, E. Ramasamy, D.Y. Lee, J.S. Song, ACS Appl. Mater. Interfaces 1 (2009) 1145—1149.
[26] G. Zhu, L. Pan, T. Lu, X. Liu, T. Lv, T. Xu, Z. Sun, Electrochim. Acta 56 (2011) 10288—10291.
[27] B.S. Lee, K.M. Park, W.R. Yu, J.H. Youk, Macromol. Res. 20 (2012) 605—614.
[28] B.S. Lee, S.B. Son, K.M. Park, W.R. Yu, K.H. Oh, S.H. Lee, J. Power Sources 199 (2012) 53—60.
[29] C. Kim, Y.I. Jeong, B.T.N. Ngoc, K.S. Yang, M. Kojima, Y.A. Kim, M. Endo, J.W. Lee, Small 3 (2007) 91—95.
[30] Y.W. Ju, G.R. Choi, H.R. Jung, C. Kim, K.S. Yang, W.J. Lee, J. Electrochem. Soc. 154 (2007) A192—A197.
[31] Y.W. Ju, J.H. Park, H.R. Jung, W.J. Lee, Electrochim. Acta 52 (2007) 4841—4847.
[32] Y.W. Ju, G.R. Choi, H.R. Jung, W.J. Lee, Electrochim. Acta 53 (2008) 5796—5803.
[33] H. Pan, C.K. Poh, Y.P. Feng, J. Lin, Chem. Mater. 19 (2007) 6120—6125.
[34] P. Lian, X. Zhu, S. Liang, Z. Li, W. Yang, H. Wang, Electrochim. Acta 55 (2010) 3909—3914.
[35] G. Veerappan, K. Bojan, S.W. Rhee, ACS Appl. Mater. Interfaces 3 (2011) 857—862.
[36] H. Sun, Y. Luo, Y. Zhang, D. Li, Z. Yu, K. Li, Q. Meng, J. Phys. Chem. C 114 (2010) 11673—11679.
[37] S.H. Park, H.R. Jung, B.K. Kim, W.J. Lee, J. Photochem. Photobiol. A 246 (2012) 45—49.
[38] T. Battumur, S.H. Mujawar, Q.T. Truong, S.B. Ambade, D.S. Lee, W. Lee, S.H. Han, S.H. Lee, Curr. Appl. Phys. 12 (2012) e49—e53.